AIP | Review of Scientific Instruments

Towards the development of a hybrid-integrated chip interferometer for online surface profile measurements

P. Kumar, H. Martin, and X. Jiang

Citation: Review of Scientific Instruments **87**, 065103 (2016); doi: 10.1063/1.4952952
View online: http://dx.doi.org/10.1063/1.4952952
View Table of Contents: http://scitation.aip.org/content/aip/journal/rsi/87/6?ver=pdfcov
Published by the AIP Publishing

Towards the development of a hybrid-integrated chip interferometer for online surface profile measurements

P. Kumar, H. Martin, and X. Jiang
EPSRC Centre for Innovative Manufacturing in Advanced Metrology, University of Huddersfield, Huddersfield HD1 3DH, United Kingdom

(Received 2 October 2015; accepted 16 May 2016; published online 3 June 2016)

Non-destructive testing and online measurement of surface features are pressing demands in manufacturing. Thus optical techniques are gaining importance for characterization of complex engineering surfaces. Harnessing integrated optics for miniaturization of interferometry systems onto a silicon wafer and incorporating a compact optical probe would enable the development of a handheld sensor for embedded metrology applications. In this work, we present the progress in the development of a hybrid photonics based metrology sensor device for online surface profile measurements. The measurement principle along with test and measurement results of individual components has been presented. For non-contact measurement, a spectrally encoded lateral scanning probe based on the laser scanning microscopy has been developed to provide fast measurement with lateral resolution limited to the diffraction limit. The probe demonstrates a lateral resolution of ~3.6 μm while high axial resolution (sub-nanometre) is inherently achieved by interferometry. Further the performance of the hybrid tuneable laser and the scanning probe was evaluated by measuring a standard step height sample of 100 nm. *Published by AIP Publishing.* [http://dx.doi.org/10.1063/1.4952952]

I. INTRODUCTION

Advances in manufacturing have led the development of high added-value critical components featuring ultra-precision structured surfaces with nanometric surface topography which are essential for their design functionalities.[1] As such, it is vital to have proper understanding of the surfaces and their properties. Development of critical components with enhanced product complexity, precision of work pieces, and the need of controlled and efficient automated production processes in manufacturing altogether has brought up pressing demands for the development of modern metrology technologies. Closer integration of metrology tool into production process incorporating automated control loop allows significant improvement in measurement accuracy, speed, and production efficiency. Furthermore, there is a changing paradigm toward a more flexible, distributed manufacturing in which a variety of bespoke components are produced in short runs. This additional burden of flexibility requires that measurement must be at the heart of any machining platform, and thus, sensors optimised for this type of online operation are a current requirement. Key attributes for online sensors are that they are small in size and robust while ideally maintaining performance commensurate with conventional standalone measurement instrumentation. Several techniques such as contact stylus, microscopy, optical methodology, etc. have been developed to measure surface characteristics to quantify the quality of surfaces with each technique having its own specific applications.[2–8] However there are very limited methods and techniques capable of providing online measurement of surfaces at very high levels of precision and accuracy at micro-nano scale. Out of all the available technologies, optical techniques are the most suitable for embedded metrology applications because of their non-destructive, easy to use instrumentation and higher speed compared to the tactile probes.[9–11] Methods like light scattering and speckle have been developed for online measurements but they only give an indirect estimation of some surface characteristics and do not obtain the surface profile.[5,12–14] Most commonly an optical interferometry is utilized for sensitive measurements at very high precision. Various open space and fibre based online interferometry systems for surface measurements have been demonstrated.[1,15–19] These systems, especially fibre based, are extremely sensitive to external disturbances and vibrations and require complex stabilization techniques to remove measurement errors.[20] Also in terms of operating speed, they still need significant improvements.

Using integrated optics technology, it is possible to significantly reduce the device dimension by integrating various components of interferometry sensor system onto a single optical chip. It will bring both the classical advantages of optics: insensitivity to electromagnetic noise; ability for non-contact measurements; suitability for use in harsh environment; and the advantages of integration: circuit miniaturization; better reliability; the ability for mass production; and low cost.[21] While several metrology sensors based on integrated optics have been developed previously, they have been limited to distance measurements applications only.[22–25] In this paper, we report on progress toward a novel high-precision miniature sensor device (Fig. 1) for embedded surface and dimensional metrology applications constructed using hybrid photonic integration technology using a silicon-on-insulator platform. Development of constituent components of the integrated-photonic device has been presented. Details of the design, construction, and performance evaluation of the associated lateral-scanning optical probe comprising a grating and scan optics will also be reported upon. The results from the current incarnation are presented to verify the potential applicability

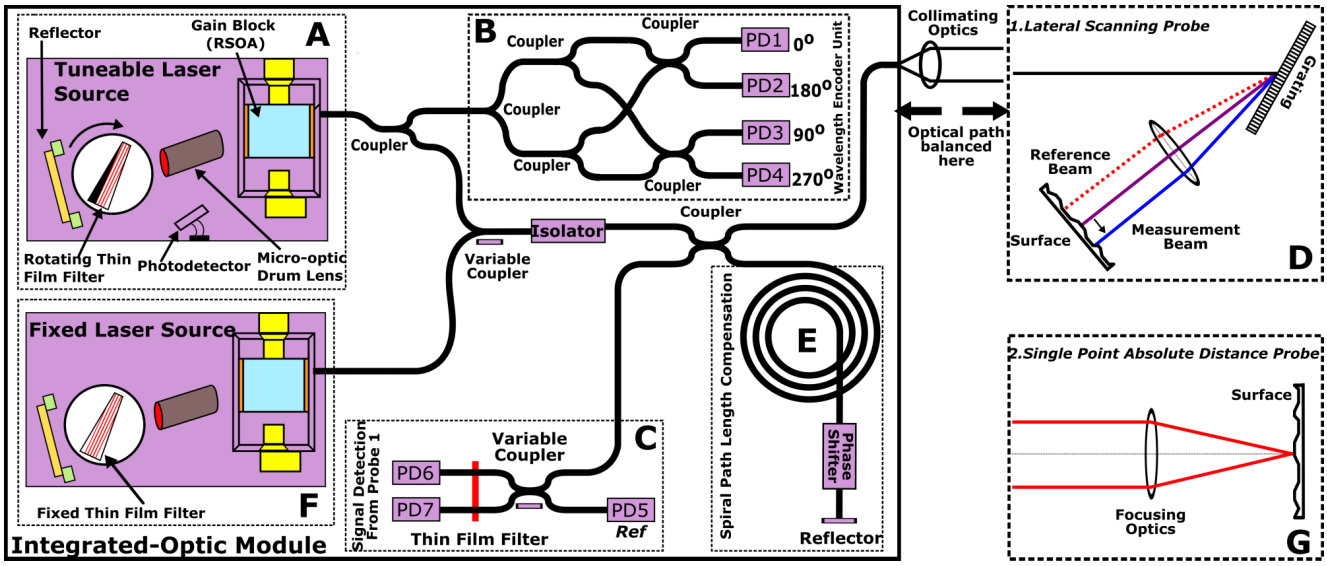

FIG. 1. Schematic of fully integrated device for online metrology application; hybrid tuneable lasers (A), wavelength encoder unit (B), signal detection unit (C), optical probe (D), phase shifting unit (E), fixed wavelength hybrid laser (F).

of this technology for an optimised device for high-precision surface profiling.

II. HYBRID PHOTONIC CHIP SENSOR

The hybrid photonic chip sensor comprises of two distinct elements: an integrated-photonic module and a separate optical probe structure. The conceptual integrated-photonic module contains all the essential components of the interferometer sensor: tuneable laser, wavelength encoder, fixed-wavelength lasers, detectors, waveguides, isolator, couplers/splitters, and a phase shifting unit (see Fig. 1). All of these elements are constructed and interconnected using hybrid-photonic integration on single silicon-on-insulator "chip." The sensor is designed to operate in two measurement modes determined by the probe type attached to the integrated-photonic part: a scanning mode, where the beam is swept across in the manner of an "optical stylus" to obtain profile measurements; a point-sensing mode, which can measure absolute distance. These two measurement modes operate using the lateral scanning probe (Fig. 1(D)) and the single point absolute distance probe (Fig. 1(G)), respectively. Absolute distance and topography measurement in the point-sensing measuring mode has been introduced previously.[26,27] Here we present the integrated-photonic "chip" sensor as a surface profiler with the lateral-scanning measurement mode. Currently some of the modules: optical isolator, phase shifting unit, and fixed laser source are still under development. However we are able to demonstrate proof-of-principle operation of the device in conjunction with the lateral scanning probe external components.

III. SENSOR MEASUREMENT PRINCIPLE

The measurement principle for the concept sensor device is based on a combination of wavelength scanning and phase shifting interferometry. In this system, the light from the tuneable laser source is coupled with a fixed laser and passed through an optical isolator after which it is split by a coupler to form the two arms of a Michelson interferometer. The fixed-wavelength laser acts as a reference wavelength source and is multiplexed into the interferometer system to track unwanted phase variations caused by environmental perturbance such as vibration or temperature drift. The reference arm is wholly on-chip and has a path length compensation spiral to equalize the lengths of the interferometer arms because of the excess length of the measurement arm path which exits the chip and transits the optical probe. Light containing the measurement arm is coupled into free space by a collimating lens where it is incident on the lateral-scanning optical probe whose first element is a grating. The 1st order diffracted beam propagates through the scan optics and objective lens to the surface of the measurand. Light returning from the reference and measurement arms re-combines at the coupler and is incident on the photodetector (PD) in the signal detection unit. Variations in surface height change the distance travelled by 1st order beam and hence change the phase at the re-combination point. The intensity introduced by the changing phase in measurement arm light can be represented by

$$I(x) = A(x) + B(x)\cos\left[\frac{2\pi}{\lambda_i(x)}(2h(x) + l)\right], \quad (1)$$

where $A(x)$ and $B(x)$ are the bias intensity and the fringe visibility at a point x on the measurand, respectively, and $h(x)$ is the height variation at that point, l is the optical path length difference between the arms of the interferometer. Further phase shifting interferometry[28] can be implemented for phase calculations as it provides high measurement accuracy and sensitivity. A stepwise phase shift is applied between the reference and test beam with an interferogram being recorded for each shift. For our application, Carré algorithm[29,30] is used because an exact phase shift is not of primary importance merely that each phase shift is of equal magnitude. This is advantageous because the phase shift is applied by moving the

reference arm mirror a physical distance, thus, the magnitude of the phase shift applies varies slightly across the wavelength range used. If $\phi(x)$ is the original phase at a sampled point x on the surface and the phase is altered by four equal steps $-3\alpha, -\alpha, +\alpha, 3\alpha$ around this point, then four intensity values $I_1(x)$, $I_2(x)$, $I_3(x)$ and $I_4(x)$ are obtained. The Carré algorithm can then be used to derive the original phase value as follows:

$$\phi(x) = \tan^{-1}\sqrt{\frac{(3I_2(x) - 3I_3(x) - I_1(x) + I_4(x))(I_1(x) + I_2(x) - I_3(x) - I_4(x))}{(I_1(x) - I_2(x) - I_3(x) + I_4(x))^2}}. \quad (2)$$

The arctangent nature of the phase calculation gives only modulo π values. To determine the phase modulo 2π, signs of quantities proportional to $\sin\phi$ and $\cos\phi$ must be evaluated from Equation (3)

$$\begin{aligned} I_2 - I_3 &= [2I_o\gamma\sin\alpha]\sin\phi \\ (I_2 + I_3) - (I_1 + I_4) &= [2I_o\gamma\cos\alpha\sin^2\alpha]\cos\phi \end{aligned}, \quad (3)$$

where γ is the intensity modulation term. The original phase value must be adjusted to as per the sign of the above quantities to lie in correct quadrant to remove the phase ambiguity. Now the phase unwrapping is implemented to obtain the actual phase value. Once the actual phase value is obtained the surface height value, h at position, x can be retrieved as follows:

$$h = \frac{\phi(x)}{4\pi}\lambda_i. \quad (4)$$

IV. SENSOR SUB-COMPONENTS

As mentioned in Section II, the development of the integrated photonics sensors has been done in an incremental fashion to facilitate ease of integration and the probability of an operational device at completion. Once all of the individual components are tested and optimized, final integration is to be undertaken to obtain a complete "chip" based sensor system. This section describes the various critical components comprising the chip interferometer system: hybrid tuneable laser (A), wavelength encoder unit (B), signal detection unit (C), the design and development of a scanning probe (D); it then concludes with a description of the final implementation and some preliminary experimental results.

A. Hybrid tuneable laser

The hybrid external cavity tuneable laser is composed of a uniform cleaved reflective semiconductor optical amplifier (RSOA), which is structured to provide the gain to the propagating mode with the front facet cleave functioning as one of the mirrors. The packaged tuneable laser is shown in the Fig. 2(a). The wavelength tuning of the laser is provided by rotating a narrowband thin film filter (TFF) in the path of a beam coming out of RSOA having first been collimated by a micro-optic drum lens. The TFF used in the module comprises a multilayer stack of dielectrics on a fused silica substrate and is capable of selecting a single longitudinal lasing cavity mode; the rotation of the TFF changes the effective dielectric stack thickness and thus selected lasing mode.

The TFF is mounted on the spindle of a of a Faulhaber brushless flat DC micro "penny" motor and rotated continuously. While the penny motor generates a maximum no-load speed of 41 740 rpm, the motor was operated at 2000 rpm (~33 Hz), which was shown to guarantee stable operation and avoided excessive heat generation. Finally, the amplified light is coupled out of the laser into the waveguide drawn on the planar lightwave circuits (PLC) via the front facet of the RSOA. Fig. 2(b) shows the laser wavelength tuning curve with respect to the angle of rotation of the TFF; the nonlinearity is due to the co-sinusoidal relationship between the

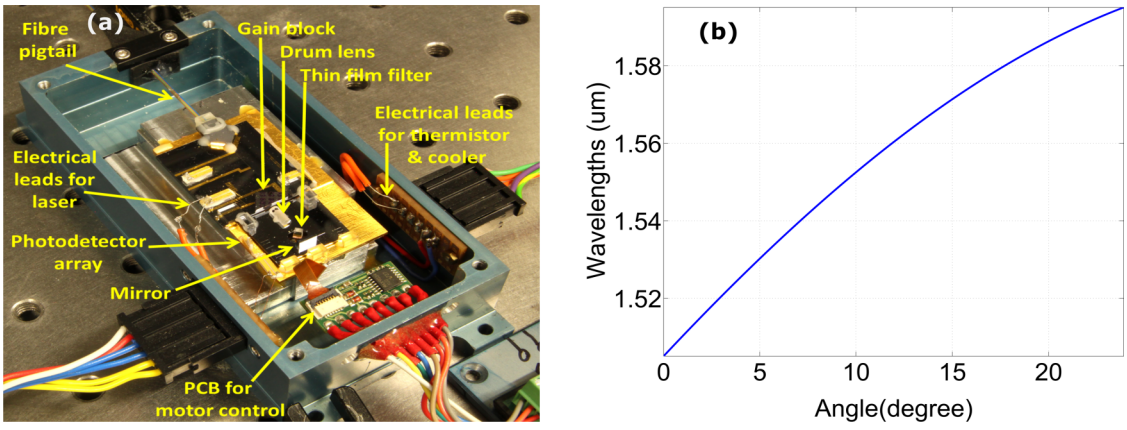

FIG. 2. (a) Packaged hybrid tuneable lasers (left) and (b) the laser tuning profile obtained using the TFF (right).

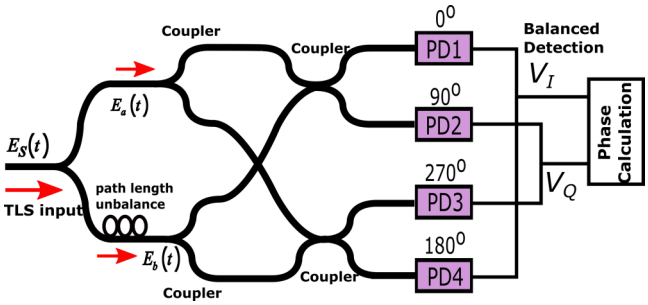

FIG. 3. Wavelength encoder unit.

effective multi-layer thickness and angle of rotation. The laser light output is transferred from the PLC waveguide to optical fibre via butt-coupling. The hybrid laser outputs power at the exit of the fibre is more than 7 dBm for an injection current of 300 mA and demonstrates single-mode operation over a spectral bandwidth of ~90 nm centred at 1550 nm. Because the Penny motor is continuously rotating, a reliable trigger signal is required for synchronous data acquisition. This is provided for by a photodiode mounted adjacent to the TFF, which picks up reflected light on each half-rotation.

B. Wavelength encoder unit

Wavelength encoder unit (Fig. 3) is a 90° optical hybrid consisting of a delay interferometer and a Mach-Zehnder interferometer configuration. An optical hybrid is multi-port devices that mix light beams and are used for coherent signal demodulation in detection. The simplest of an optical hybrid is 3 dB couplers where a phase shift of 180° is introduced in one of the branches of the output port. Similarly a 90° hybrid is a six port device with two input and four output ports, which produces several interference signals with phase difference of approximately 90°. These hybrids have been realized in all-fibre,[31] planar waveguide,[32–34] and free-space bulk optics[35] formats. Out of these, optical hybrids based on photonic light wave circuits offer compactness, low cost, and stable operation. As such, the planar waveguide based optical hybrid manufacture used for this device is the ideal technology for implementing high-speed real-time wavelength monitoring of the hybrid tuneable laser. Wavelength encoder optical hybrid is made using 2 × 2 waveguide couplers forming a Mach-Zehnder interferometer with a path length imbalance of 253.5 μm. This provides a free spectral range of ~6 nm with an adequate wavelength resolution. The photodetectors are hybrid integrated and loaded with 10 k resistors.

With reference to Figure 3, light from the tuneable laser $E_S(t)$ is fed into the wavelength encoder unit and then split to form two waves, $E_a(t)$ and $E_b(t)$. $E_b(t)$ is delayed by an extra path length ΔT such that

$$E_a(t) = E_s(t) = |E_s(t)|\, e^{j\theta_s(t)} \tag{5}$$

$$E_b(t) = E_s(t - \Delta T) = |E_s(t - \Delta T)|\, e^{j\theta_s(t-\Delta T)}, \tag{6}$$

where θ is the phase of individual waves. The phase difference between these two waves is given by

$$\Delta\theta(t) = \theta_s(t) - \theta_s(t - \Delta T). \tag{7}$$

The four phase-quadrature signals obtained at the output are detected by corresponding photodiodes arranged in an array. Balanced detection scheme in which the signals from a pair of photodiodes cancel was implemented for signal demodulation to obtain good signal to noise ratio. Balanced detection is more sensitive and can detect low power signals as well as eliminates the noise from electrical signal. Assuming all the photodiodes have the same responsivity R, the resulting differential signals; in-phase (V_I) and quadrature (V_Q) can be given as

$$V_I = RE_aE_b \cos[\Delta\theta(t)] \tag{8}$$

$$V_Q = RE_aE_b \sin[\Delta\theta(t)]. \tag{9}$$

The signals obtained from the balanced detection scheme are demodulated by arctangent computation using the following formula:

$$\theta_{phase} = \tan^{-1}\left(\frac{V_I}{V_Q}\right). \tag{10}$$

For precise quadrature detection, it is important that the power outputs are balanced and phase difference is 90°; however, variation during fabrication tends to conspire against this ideal scenario leading to inaccuracies in phase determination.

To test the encoder module, the hybrid tuneable laser used as a source, a tap-coupler directs 10% of the laser power to the wavelength encoder unit for wavelength monitoring during the tuning process. The tuneable laser was scanned over its full range, allowing the beam to propagate through the encoder unit. The four photodetector outputs of the encoder are shown in Fig. 4(a), the expected sinusoidal response resulting from the wavelength tuning is clear to see. The instantaneous phase of individual signals was calculated by using a Fourier transform based technique.[36] Fig. 4(b) and Table I show the relative instantaneous phase difference between the outputs of each of the ports with respect to PD1.

The phase relative phase shift is observed to vary up to ±12°, which is mainly due to variations in the waveguide core reproducibility and homogeneity during fabrication. The obtained four quadrature signals from the photodetector were then postprocessed in Matlab. The DC component from the signals was eliminated and the gain offset adjustment was performed.

The phase obtained using the Equation (10) had discontinuities, which was then unwrapped to get the actual phase information shown in Fig. 5. The phase change correlates with the wavelength tuning and resembles with the tuning curve shown in Fig. 2 (right). Some discontinuities in phase are clearly evident which can be attributed to the power mismatch between the signals though it should be noted that these are systematic. Ideally the generated phase curve needs to be calibrated against an external tuneable laser source so it can be correlated against known wavelengths. Once calibrated, the phase information can be used to monitor the wavelength tuning of the hybrid tuneable laser in real-time.

C. Signal detection unit

The signal detection unit is a PLC comprising a coupler, a pair of thermo-optic phase shifters, TFF, and a photodetector

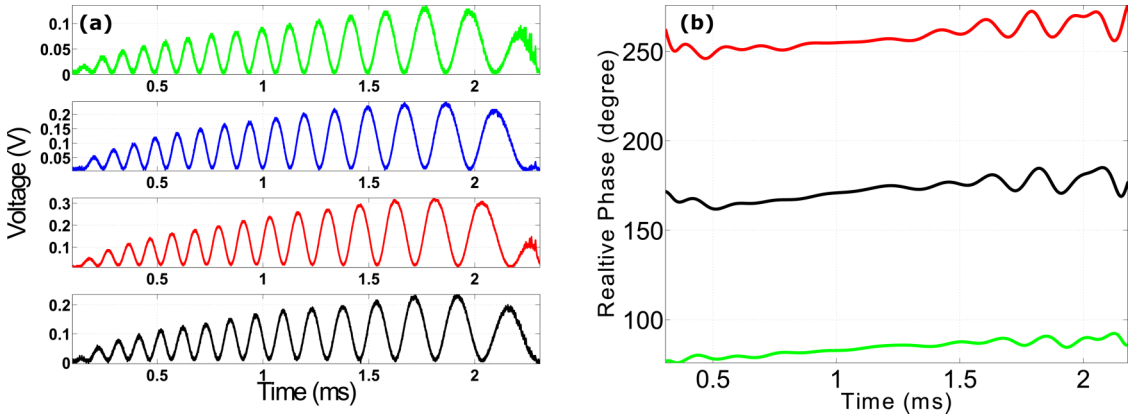

FIG. 4. (a) Response from the individual photo-detectors (PD1, PD2 PD3, and PD4) and (b) relative phase difference at the output ports of the wavelength encoder with respect to the PD1.

array (Fig. 6). Because the output of the interferometer contains a multiplexed signal from both a tuneable laser source and a fixed wavelength source, a TFF having high transmission of the wavelength range of the former and high reflectivity at that of the latter is used to reflect the reference light back out to PD5. Light from the tuneable laser source passes to PDs 6 and 7, and as they are anti-phase will be measured using a balanced detection scheme.

To test the detection unit, an external tuneable laser (HP 8168 F) was used. The HP laser was tuned stepwise manually from 1480 nm to 1580 nm in increments of 1 nm. The output from the laser (measurement signal) was fed into the signal detection unit via a fibre port coupled to input waveguide on the PLC. The response of the photodetectors was measured using a voltmeter across a 10 k load resistor. The response of the photodetectors at an input power of 0.5 mW is shown in the Fig. 7.

PD6 and PD7 have a clean cutoff below 1490 nm; the variation in the passband responses is due to the gain mismatch arising from variances in the manufacturing process. The response of PD5 shows that there is still some leakage of the tuneable laser source at longer wavelengths of the scan. The reference beam, which is reflected from the filter and incident on PD5, appears to have a good response in the pass band region below 1490 nm. However there is substantial ripple present in the stop band amounting to almost 10% power at the peaks.

D. Spectrally encoded lateral scanning probe

Several approaches to beam scanning have been demonstrated such as scanning galvo-mirrors (including MEMS devices), and proximal scanning of single-mode fibre bundles has been devised and implemented to scan the beam in orthogonal directions onto the object plane.[37–44] The majority of scanning probing systems developed so far have been limited to biomedical or endoscopic imaging applications only, except the few developed for surface metrology such as confocal scanning probe. The major drawbacks of these spot scanning techniques are that the off-axis lens aberration must be minimized and corrections are required for the off-axis light transmission reduction.[37] Also because of the mass of the elements and the resulting inertia in the mechanical scanners used, there is a limit to the rate at which beams can be scanned. To overcome the above limitations of mechanical scanners, a spectrally encoded lateral scanning optical probe is presented consisting of a dispersive optical element and an objective to provide high-speed raster scanning of the focused beam over the measurand by tuning the source light wavelengths supplied by the hybrid tuneable laser. By tuning the wavelength of the tuneable laser and by suitably selecting a grating, it is possible to steer the beam of light at different angles following the grating equation:

$$d(\sin\alpha + \sin\beta) = m\lambda \qquad m = 0, \pm1, \pm2, \ldots, \qquad (11)$$

where λ is the wavelength of light, d is the grating pitch or groove spacing, α is the incident angle, β is the diffraction

TABLE I. The mean phase difference between the output ports of the wavelength encoder.

	Mean value of relative phase difference with respect to PD1(deg)	Ideal relative phase difference (deg)	Error (deg)
PD2	172.61	180	7.38
PD3	258.23	270	11.76
PD4	84.30	90	5.69

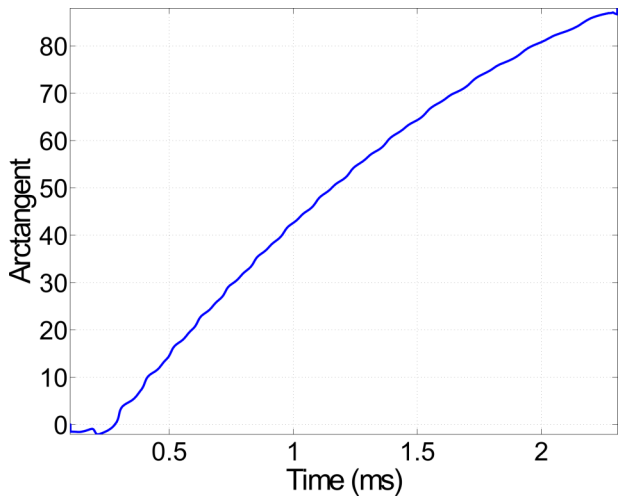

FIG. 5. Estimated phase value obtained from the encoder.

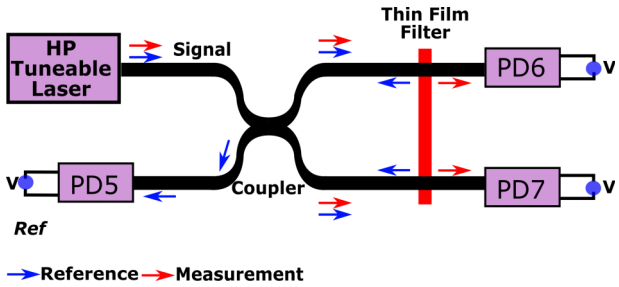

FIG. 6. Measurement setup for the signal detection unit.

angle, m is the diffraction order. The configuration of the spectrally encoded lateral scanning probe is presented in Fig. 8. The optical probe consists of a fibre collimator, grating, scan lens, tube lens, and infinity-corrected microscope objective. The tunable laser source (TLS) launches light into single mode fibre having a core diameter of ~4 μm. It must be noted here that the core of the single mode fibre acts as both a source and detector pinhole. A high numerical aperture (NA) collimating lens maximizes the coupling between the fibre and the collimator lens. This will in turn minimize the confocality thus providing access to the full depth-of-focus of the microscope objective.

In our apparatus, the output beam from the single mode fibre was collimated using a fibre collimator (Thorlabs, Inc., TC06APC-1550, 0.28 NA, f = 6 mm), which is incident on the grating (Edmund Optics, 830 lines/mm). The diffraction grating is positioned at the back focal plane of the scan lens SL (Thorlabs, AC080-016-C-ML), which deflects the beam across its entrance aperture in raster fashion. The optical axis of the probe system is aligned such that it is coaxial to the dispersed beam at the central operational wavelength of 1550 nm (λ_c). Another beam at any wavelength λ_i makes an angle, $\Delta\beta_R = \beta_{\lambda_c} - \beta_{\lambda_i}$ with the optical axis, as defined by the axis of propagation of the beam at the central wavelength.

The scan lens converts the angularly dispersed beam into linear deflection of focussed spot in primary image plane. The tube lens TL (Thorlabs, AC254-050-C-ML) is positioned at its back focal length from the primary image plane forming an afocal Keplerian system, which acts as a beam expander

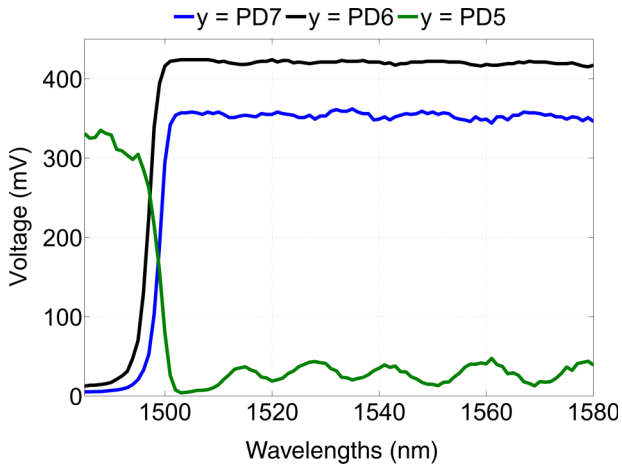

FIG. 7. PD response over the wavelength scan.

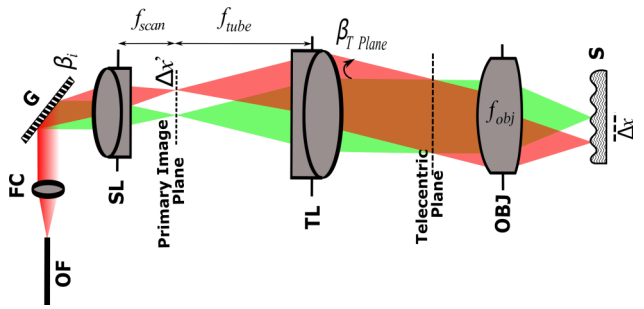

FIG. 8. Lateral scanning probe configuration. (OF—optical fibre, FC—fibre collimator, G—grating, SL—scan lens, TL—tube lens, OBJ—objective lens, S—sample).

increasing the beam diameter to 8.25 mm almost filling the back aperture of the objective lens (10× Mitutoyo Plan Apo NIR Infinity-Corrected Objective, NA = 0.26, f = 20 mm). An afocal Keplerian system consists of two positive lenses positioned such that their focal lengths are coincident. The focal lengths of lenses are chosen such that the exiting beam is expanded to the desired extent. The linear scan by the SL is reconverted into angular scan by the TL about a pivot point located on the optical axis intersecting with the front focal plane of the tube lens called the telecentric plane. Thus the angle ($\beta_{T\ Plane}$) in the telecentric plane provided by TL is related to the relative diffraction angle (β_R) given by

$$\beta_{T\ Plane} = \frac{f_{scan}}{f_{tube}} \times \beta_R. \tag{12}$$

Finally the beam passing through the microscope objective lens hits the sample target. The back filling of objective by the beam expander maximizes the object-space numerical aperture (NA) of the optical system consequently achieving diffraction limited spot size for maximal resolution. In addition to increasing the object space NA, the beam expander also translates the actual "pivot" point on the diffraction grating to a virtual pivot point located at the back focal plane of the objective lens. This action results in the objective lens converting the angular scan about the virtual pivot point into linear scan across the sample as described by

$$\Delta x = f_{obj} \times \tan \beta_{T\ Plane}. \tag{13}$$

The retro-reflected light from the sample retraces its path through the optical probe system and is collected back at the fibre collimator whereupon it is directed to a photo-detector via a circulator.

1. System optical performance

a. Lateral resolution. The approximate lateral resolution of a conventional microscope objective may be given by

$$d_{\min} \approx \frac{1.22\lambda}{2NA} = \frac{0.6\lambda}{NA}, \tag{14}$$

where λ is the wavelength of light and NA is the numerical aperture of the microscope objective. Thus the 0.26 NA microscope objectives in use would achieve a theoretical resolution of approximately 3.6 μm at an illumination wavelength of 1.55 μm. Because the lateral scan is provided through the

angular deflection of the input beam using a diffraction grating, the spectral resolution of the device will depend on both the grating as well as the linewidth of the laser used. The hybrid tuneable laser has a longitudinal mode spacing of 0.04 nm and a bandwidth of 90 nm and can therefore the system can resolve 2250 discrete points along the line-scanned profile. The resolving power of the grating in the imaging arm is given by equation

$$R = \frac{\lambda}{\Delta\lambda} = \frac{mD}{\Lambda}, \quad m \text{ being the order,} \tag{15}$$

where $\Delta\lambda$ is the spectral resolution of the grating, m is the order of diffraction, Λ is the period of the grating, and D is the diameter of the beam. Thus the resolving power of the grating is directly proportional to the incident beam diameter on the grating and inversely proportional to the grating frequency Λ.[20] A beam of diameter $D = 1.2$ mm/ $\cos(63^\circ) = 2.64$ mm at wavelength $\lambda = 1550$ nm is made incident onto 830 line/mm grating will have first order spectral resolution of

$$\Delta\lambda = \frac{\Lambda \times \lambda_{1550\text{nm}}}{D} = \frac{1.204 \times 10^{-6} \times 1.5510^{-6}}{2.64 \times 10^{-3}} = 0.706 \text{ nm}. \tag{16}$$

This corresponds to approximately 130 resolved points. Thus the resolution of the system is limited by optical resolution as long as the field of view (FOV) is less than approximately $130 \times 3.57\ \mu\text{m} = 464.1\ \mu\text{m}$.

b. Measurement range. The hybrid tuneable laser provides ~±45 nm of wavelength tuning on either side of the central wavelength. The maximum scan angle ($\Delta\beta_R{}^{\max}$) provided by the diffraction grating is the angle difference between the beam at central wavelength and the extreme wavelength on either side of the tuneable laser bandwidth and is given by the equation

$$\Delta\beta_{R_{\max}} = \beta\lambda_c - \beta\lambda_{i(\text{end/start})}. \tag{17}$$

This in turn provides a maximum tilt angle $\beta^{\max}{}_{T\ Plane}$ of the beam in the telecentric plane given by Equation (6), which defines the outermost position of the scanned spot in the object plane in relation to the central wavelength position. Considering linear dispersion of grating, twice the linear scan defined by Equation (7) will give full lateral scan range or the field of view (FOV) in the object plane represented by

$$FOV = 2 \times \Delta x = 2 \times f_{obj} \times \tan \beta^{\max}{}_{T\ Plane}, \tag{18}$$

where f_{obj} is the focal length of the objective lens and $\beta^{\max}{}_{T\ Plane}$ is the maximum tilt angle in the telecentric plane.

2. Optical probe characterization

a. Knife edge experiment. The lateral resolution of the scanning probe was empirically measured using a knife-edge test. The Gaussian beam here in this case is not radially symmetric because of the astigmatism produced by the grating and so a measurement of beam radius was obtained in orthogonal directions aligned with the major and minor axes. The spot size of the beam was measured at different positions associated with specific tuned wavelengths. The knife edge was scanned through the focal point of the beam, perpendicular to the axis of propagation, while the transmitted intensity was recorded using a photo-detector. For a Gaussian beam in a beam scanning system, the lateral resolution is defined as its $1/e^2$ radius and is approximately $0.78 \times 10\%$-90% edge width of the transmission profile obtained at detector when the knife edge is moved across the beam. The calculated values of spot sizes at different wavelengths are shown in Fig. 9, respectively. At the central wavelength (1550 nm), the spot is close to the theoretical value calculated using Rayleigh criteria. Off-axis aberration dominated by astigmatism due to the grating element quickly degrades the resolution on either side of the wavelength scan because of increased scan angle.

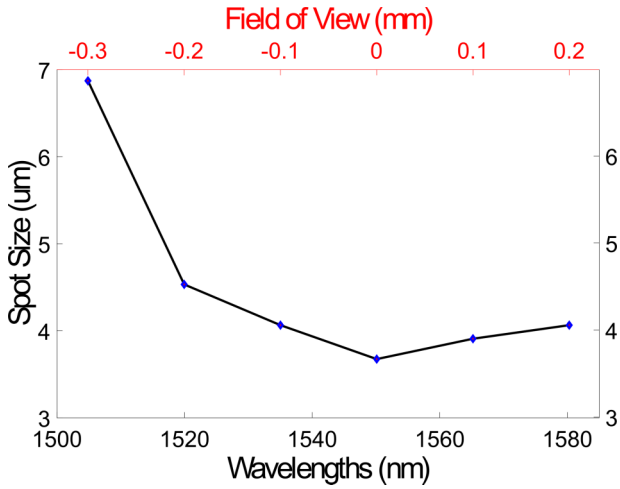

FIG. 9. Plot of spot size measured along transverse direction (Y) at different wavelengths using knife edge experiment.

A USAF resolution target was also used to confirm the optical resolution of the probe system. The sizes of individual elements of group 7 elements are given in the Table II. The USAF target consists of lithographically generated high contrast features of precisely defined width and spacing defined in groups. Fig. 10 shows the sample, the black chrome coated highly reflective areas, while the white areas are the uncoated glass substrate having lower reflectivity. The usable resolution can be determined by analysing the intensity modulation obtained when the beam is scanned across the target. An assumption of 50% modulation in the recorded intensity was taken as the limit for the resolving of adjacent features. The resolution test target was placed at the focus plane of the objective and normal to the optical axis of the probe. A photo-detector was used to detect the reflected light intensity returning from the test target via a circulator.

TABLE II. Size chart of group 7 elements.

USAF 1951 resolution target group 7 elements (E)	Element size (μm)
1	3.90
2	3.47
3	3.11
4	2.76
5	2.46
6	2.19

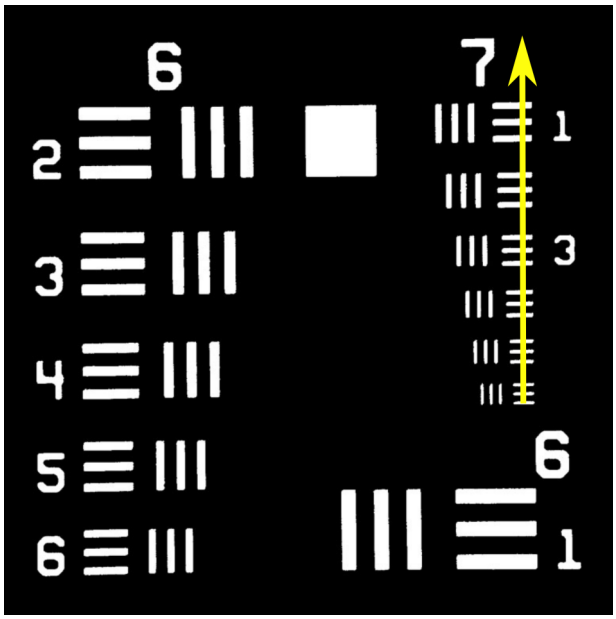

FIG. 10. The image showing line scanned across the group 7 elements of a 1951 USAF resolution target test.

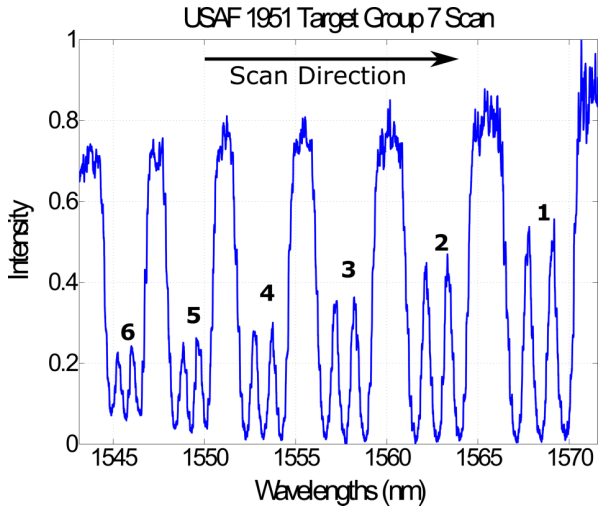

FIG. 11. Intensity measured as the beam was scanned across all elements of group 7 on the USAF target, as denoted by the yellow line in Fig. 10. Element numbers are labelled, with the widest being at the end to the scan, on the right hand side.

Fig. 11 is an intensity modulation plot of the group 7 scan taken along the line shown in Fig. 10. The intensity minima correspond to the lower reflectivity features (shown in white in Fig. 10). An increase in intensity modulation between the features is apparent from left to right with as the feature width increases. The previously outlined 50% intensity modulation requirement for a fully resolved feature is clearly met by element 1 (3.9 μm width) while element 2 (3.47 μm width) appears borderline. This result correlates well with the theoretical and knife edge resolution tests results for beam width described earlier. The more slowly varying increase in intensity apparent from left to right in Fig. 11 is predominantly due to the gain profile for the tuneable laser source, which has higher power at longer wavelengths.

V. SURFACE PROFILE MEASUREMENT

To demonstrate the feasibility of the developed optical scanning probe for surface profilometry, the experimental setup shown in Fig. 12 was used to measure a step height standard supplied by National Physical Laboratory (NPL), UK. Figs. 13(a) and 13(b) show a 3-D and 2-D cross-sectional profile, respectively, of the step height sample as measured by Taylor Hobson Coherence Correlation Interferometry (CCI)

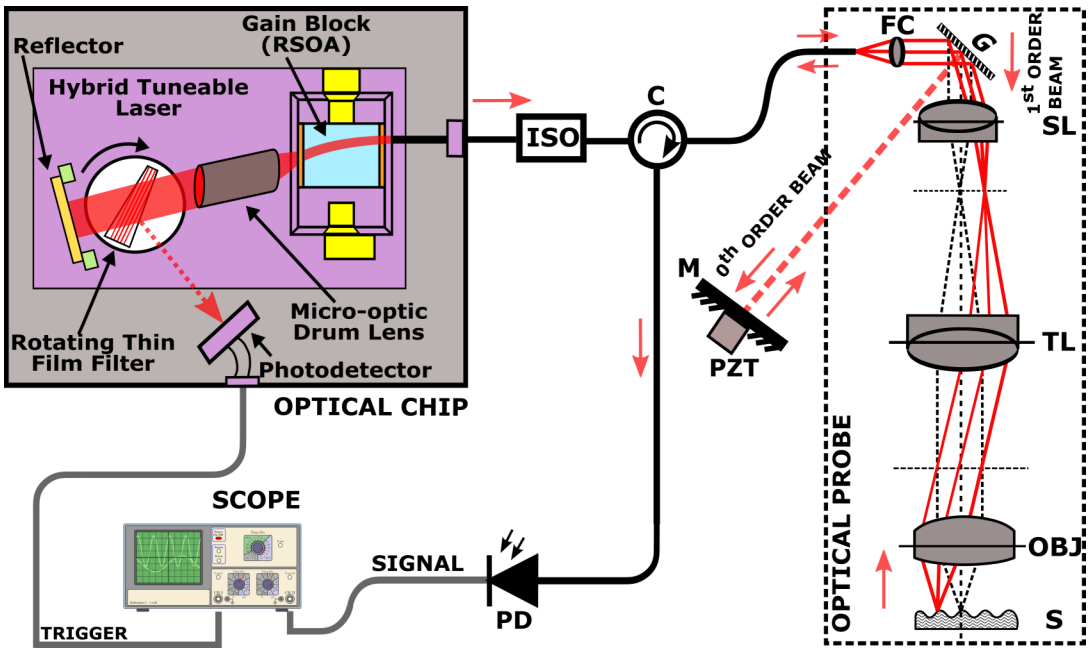

FIG. 12. Schematic of the surface profile measurement setup (scanning probe system with hybrid tunable laser). Black line—fibre/waveguide, Brown—electrical line. (ISO—isolator, C—circulator, FC—fiber collimator, G—grating, SL—scan lens, TL—tube lens, OBJ—objective lens, S—sample, M—mirror, PD—photodetector).

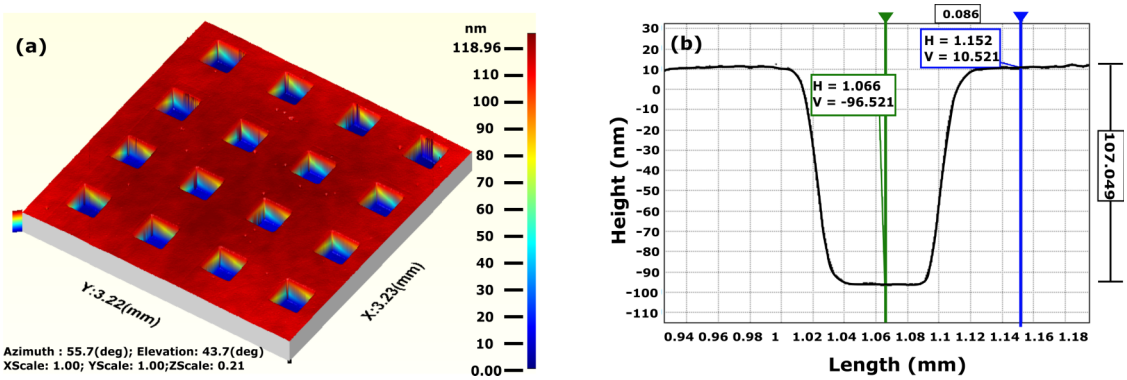

FIG. 13. (a) Standard NPL artefact sample and (b) Sample cross section profile.

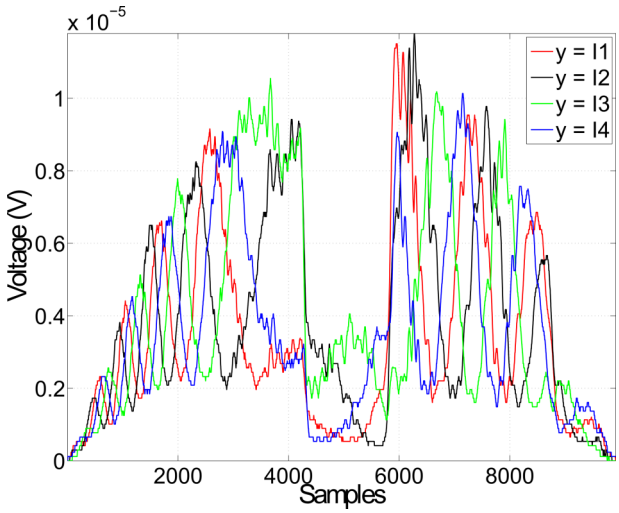

FIG. 14. Four phase shifted interferogram signals.

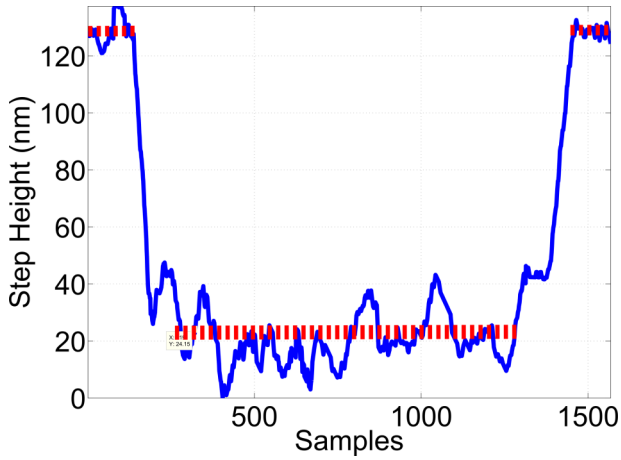

FIG. 15. Step height measured by lateral scanning probe.

instrument using a 5× objective. The measured step height of the sample was found to be ~107 nm.

Light from the tuneable laser propagates into the scanning probe system via the circulator. The zeroth order beam reflected off the grating (G) was taken as the reference beam for the purpose of generating interference. The first order beam forms the measurement arm and propagates through the lateral scanning probe to the sample. The two reflected beams interfere back on grating where the resulting interfered beam is coupled back into the fiber, and via the circulator, is incident on a photodetector (PD). For synchronous data acquisition, a photodiode is mounted onto the optical chip to pick a portion of reflected beam from the TFF to be used for trigger signal. The data were acquired with an oscilloscope and post-processed with Matlab to obtain the measurement results.

The Carré algorithm outlined in Section III was implemented to retrieve the phase information from the interferogram data and thus deduce the surface profile. In order to shift the phase, a piezoelectric transducer (PZT P-840, Physik Instrumente) was attached to the mirror in the reference arm and was controlled by computer in order to produce the required translations. The four phase shifted interferograms as obtained from the step height standard are shown in Fig. 14.

The obtained phase was then unwrapped to get the final phase value, which was used for the calculation of the height. Fig. 15 shows the profile of the step height standard as measured using this experimental setup. The step height obtained was ~108 nm. Although higher level of noise is observed in scanning probe measurement as compared to the CCI measurement in Fig. 12, the overall absolute step height measurement correlated with that obtained from the commercial instrument.

VI. CONCLUSION

The progress in the development of an integrated photonic sensor for surface and dimensional measurement has been presented. Individual core sub-systems including a tuneable laser, wavelength encoder unit, signal detection unit, and a scanning probe system have been developed individually and tested. The wavelength encoder unit appears operable but there is significant amount of systematic phase error observed between the output signals. The signal detection unit is operational and the measurement signal path is working well; however, some ripples have been observed in the reflected reference signal in the stop band. A bench top prototype of spectrally encoded lateral scanning probe was designed and investigated for surface profile measurement using the integrated photonic sensor. Initial characterization of the lateral scanning probe was performed using the knife edge experiment and the USAF resolution test target. An experimental apparatus was used to make a profile measurement so that the principle of using

an integrated photonic sensor for surface metrology could be verified within the limitations set by the technical issues that occurred during fabrication and assembly.

VII. FUTURE WORK

Future work will involve performance improvements in the existing modules of integrated photonic interferometer as well as the development and integration of the phase shifting unit, fixed wavelength reference laser source, and detectors. In the wavelength encoder module, the phase offset error will be characterised and subsequently reduced to achieve more accurate wavelength information during the scanning. The signal detection unit design will be optimised to suppress leakage of the reference light into the wavelength scanning range passband. For phase shifting in the reference arm, an array of RSOAs optimised for fast switching is to be integrated onto the optical chip. The prototype probe developed requires further size reduction, which will be achieved using micro-optics technology and path length optimisations with beam folding schemes to reduce the overall probe volume. Finally, once the successful integration of all the optimised core modules of the interferometry system is complete, the metrology characteristics of the device will be carried out using a variety of artefacts, thus providing an indication of real-world performance in measurement applications.

ACKNOWLEDGMENTS

The authors would like to acknowledge the Centre for Integrated Photonics (CIP), Ipswich, UK for their contribution to this work through the manufacture of the photonic devices reported in this paper. The authors also gratefully acknowledge the European Research Council Surfund Project (No. ERC-228117) and the UK's Engineering and Physical Sciences Research Council (EPSRC) funding of the EPSRC Centre for Innovative Manufacturing in Advanced Metrology (Grand No. EP/I033424/1).

[1]X. Jiang, "Precision surface measurement," Philos. Trans. R. Soc., A **370**, 4089 (2012).
[2]D. J. Whitehouse, *Handbook of Surface and Nanometrology* (CRC press, 2010).
[3]R. J. Hocken, N. Chakraborty, and C. Brown, CIRP Ann. - Manuf. Technol. **54**, 169 (2005).
[4]C. Y. Poon and B. Bhushan, Wear **190**, 76 (1995).
[5]T. Vorburger and E. Teague, Precis. Eng. **3**, 61 (1981).
[6]M. Conroy and J. Armstrong, in *Proceedings of Journal of Physics: Conference Series* (IOP Publishing, 2005).
[7]S. H. Ali, ISRN Opt. **2012**, 1.
[8]J. C. Wyant and K. Creath, Int. J. Mach. Tools Manufac. **32**, 5 (1992).
[9]T. V. Vorburger, H.-G. Rhee, T. B. Renegar, J.-F. Song, and A. Zheng, Int. J. Adv. Manufac. Technol. **33**, 110 (2007).
[10]S. Thian, W. Feng, Y. Wong, J. Fuh, H. Loh, K. Tee, Y. Tang, and L. Lu, in *Proceedings of Journal of Physics: Conference Series* (IOP Publishing, 2007).
[11]T. Mathia, P. Pawlus, and M. Wieczorowski, Wear **271**, 494 (2011).
[12]R. D. Young, T. V. Vorburger, and E. C. Teague, CIRP Ann. - Manufac. Technol. **29**, 435 (1980).
[13]R. Brodmann, T. Gast, G. Thurn, A. Wirtz, and O. W. G. Rodenstock, CIRP Ann. - Manufac. Technol. **33**, 403 (1984).
[14]U. Minoni and F. Cavalli, Measurement **41**, 774 (2008).
[15]H. Martin and X. Jiang, Opt. Lett. **35**, 655 (2010).
[16]I. Alvarez, J. M. Enguita, J. Marina, and C. Fraga, Opt. Eng. **47**, 023602 (2008).
[17]J. M. Enguita, I. Álvarez, M. Frade, and J. Marina, Opt. Eng. **49**, 023602 (2010).
[18]I. Alvarez, J. M. Enguita, M. Frade, J. Marina, and G. Ojea, Sensors **9**, 7021 (2009).
[19]X. Jiang, K. Wang, F. Gao, and H. Muhamedsalih, Appl. Opt. **49**, 2903 (2010).
[20]D. A. Jackson, R. Priest, A. Dandridge, and A. B. Tveten, Appl. Opt. **19**, 2926 (1980).
[21]S. Valette, S. Renard, J. Jadot, P. Gidon, and C. Erbeia, Sens. Actuators, A **23**, 1087 (1990).
[22]S. Ura, M. Shinohara, T. Endoh, H. Nishihara, and T. Suhara, Electron. Commun. Jpn. (Part II: Electron.) **77**, 13 (1994).
[23]T. Suhara, T. Taniguchi, M. Uemukai, H. Nishihara, T. Hirata, S. Iio, and M. Suehiro, IEEE Photon. Technol. Lett. **7**, 1195 (1995).
[24]T. Lang, D. Genon-Catalot, P. Dandrea, I. S. Duport, and P. Benech, J. Opt. **29**, 135 (1998).
[25]T. Ito, R. Sawada, and E. Higurashi, J. Micromech. Microeng. **13**, 942 (2003).
[26]P. Kumar, H. Martin, G. Maxwell, and X. Jiang, Proc. SPIE **8988**, 898801 (2014).
[27]H. Martin, P. Kumar, and X. Jiang, CIRP Ann. - Manufac. Technol. **63**, 549 (2014).
[28]K. Creath, Prog. Opt. **26**, 349 (1988).
[29]P. Carré, Metrologia **2**, 13 (1966).
[30]Q. Kemao, S. Fangjun, and W. Xiaoping, Meas. Sci. Technol. **11**, 1220 (2000).
[31]L. G. Kazovsky, L. Curtis, W. C. Young, and N. K. Cheung, Appl. Opt. **26**, 437 (1987).
[32]M. Seimetz and C.-M. Weinert, J. Lightwave Technol. **24**, 1317 (2006).
[33]L. Zimmermann, K. Voigt, G. Winzer, K. Petermann, and C. M. Weinert, IEEE Photon. Technol. Lett. **21**, 143 (2009).
[34]S.-H. Jeong and K. Morito, Opt. Express **18**, 8482 (2010).
[35]Y. Zhou, J. Sun, A. Yan, Z. Luan, L. Wang, and L. Liu, Proc. SPIE **7464**, 746410 (2009).
[36]C. Gorecki, Pure Appl. Opt.: J. Eur. Opt. Soc. Part A **1**, 103 (1992).
[37]P. M. Delaney, M. R. Harris, and R. G. King, Appl. Opt. **33**, 573 (1994).
[38]J. Pawley, *Handbook of Biological Confocal Microscopy* (Springer Science & Business Media, 2010).
[39]T. Dabbs and M. Glass, Appl. Opt. **31**, 3030 (1992).
[40]D.-H. Kim, I. K. Ilev, and J. U. Kang, IEEE J. Sel. Top. Quantum Electron. **14**, 82 (2008).
[41]M. R. D. Chen Liang, K.-B. Sung, and R. Richards-Kortum, Opt. Express **9**, 821 (2001).
[42]C. Boudoux, S. Yun, W. Oh, W. White, N. Iftimia, M. Shishkov, B. Bouma, and G. Tearney, Opt. Express **13**, 8214 (2005).
[43]H.-J. Shin, M. C. Pierce, D. Lee, H. Ra, O. Solgaard, and R. Richards-Kortum, Opt. Express **15**, 9113 (2007).
[44]K. Kumar, R. Avritscher, Y. Wang, N. Lane, D. C. Madoff, T. K. Yu, J. W. Uhr, and X. Zhang, Biomed. Microdevices **12**, 223 (2010).